Nanoscale

PAPER

View Article Online
View Journal | View Issue

Cite this: *Nanoscale*, 2025, **17**, 24529

Effects of surface functionalization and size of MXene-based quantum dots on their optical properties: the exciton confinement matters

Barbora Vénosová and František Karlický *

In this study, we explore the influence of surface functionalization and quantum dot size on the electronic and optical properties of MXene quantum dots (MXQDs) using time-dependent density functional theory. Our findings demonstrate that surface terminations have a significant influence on the electronic and optical properties of Ti_2CT_2 (T = O, F, OH) MXQDs. Different functional groups induce notable shifts in both the energy gap and the absorption spectrum. The oxygen termination yields the highest stability and the largest energy gap, while hydroxyl and fluorine terminations shift absorption toward the visible and near-infrared regions. The study also reveals a pronounced blue shift in the absorption spectrum as the Ti_2CO_2 QDs shrink. In addition, small quantum dots with a lateral size of ~1–2 nm exhibit strong quantum coupling effects, accompanied by an increase in exciton binding energy with delocalization across the quantum dot. The binding energy of the first exciton in MXQDs can achieve up to 75% of its energy gap (in corresponding 2D materials, the typical value is around 25%), which critically influences (increases and shifts) optical absorption.

Received 23rd July 2025,
Accepted 2nd October 2025

DOI: 10.1039/d5nr03127c

rsc.li/nanoscale

1 Introduction

In 2011, Gogotsi and Barsoum[1] discovered a novel class of 2D materials known as MXenes, synthesized by selectively etching the A-layer atoms from the MAX phase. These materials are described by the general chemical formula $M_{n+1}X_nT_x$ ($1 \leq n \leq 4$ and $x \leq 2$), where M denotes a transition metal atom (*e.g.*, Ti, V, Sc, Mo, Ta, or Nb), X denotes carbon or nitrogen atoms and T represents surface terminal groups like –O, –OH, –F and/or atoms from groups 16 and 17 of the periodic table.[2] MXenes exhibit a planar morphology with remarkable surface properties, high structural stability, excellent electrical conductivity, and tunable thermal, mechanical, optical, and chemical characteristics. Despite the emergence of interesting phases such as semiconductors,[3] excitonic insulators,[4] and antiferromagnets,[5] the majority of MXenes exhibit metallic conductivity without an intrinsic energy gap. This behavior is largely attributed to the presence of end groups (*e.g.*, –F and –OH) that close the energy gap and restrict their tunability, thereby limiting their use in optoelectronic and photonic devices.[6–9] One promising strategy to address this limitation involves reducing the lateral dimensions of MXenes to form nanoribbons or quantum dots (QDs).[10–12]

Quantum dots (QDs), classified as zero-dimensional materials with sizes typically ranging from 1 to 10 nm, can exhibit small dimensions that introduce spatial constraints, potentially limiting exciton behavior depending on their size and material composition. This unique characteristic gives rise to a broad range of properties, notably the quantum confinement effect, visible-light absorption, and diverse surface-active sites, making them promising candidates for applications in catalysis and energy conversion.[13–15] The quantum confinement effect arises when the size of a QD approaches or becomes smaller than the exciton radius, *i.e.*, the characteristic distance between an electron and a hole separation, in the corresponding 2D material. Under such conditions, carrier motion is restricted in all three spatial directions, producing discrete quantum states rather than the continuous bands of an extended 2D system. As a result, the band gap increases and the electronic/optical properties become strongly size-dependent.[16,17] This size dependence allows precise tuning of absorption and emission wavelengths simply by adjusting the particle size.[15,18,19] Smaller quantum dots, where confinement is strongest, typically display a blue shift in their absorption spectra, while larger dots behave more like the parent 2D material.[20–26] The blue shift observed in smaller QDs is a direct consequence of the confinement effect, where excitons generated by electron–hole pairs are more delocalized across the quantum dot compared to the corresponding 2D material, impacting the optical properties of nanostructures.[27–29] For example, Drissi *et al.*[30] have demonstrated a significant effect of particle size on the optoelectronic properties of graphene, graphene-based silicon, and diamond quantum dots. They

Department of Physics, Faculty of Science, University of Ostrava, 30. dubna 22, 7013 Ostrava, Czech Republic. E-mail: frantisek.karlicky@osu.cz; Tel: +420 553 46 2155

observed a redshift of absorption peaks with increasing particle size, accompanied by a decrease in exciton binding energy. Madden and Zwijnenburg[27] also found that in hydrogenated silicon nanoparticles, fundamental, optical gaps, and exciton binding energy increase with reduced particle size, while excitons remain delocalized within the particle. At the same time, they showed that the average distance between the hole and the electron increases in proportion to the particle size. Elward and Chakraborty[28] have investigated the influence of CdSe quantum dot size on exciton binding energy and the electron–hole recombination probability. Their findings show that both the exciton binding energy and the probability of electron–hole recombination decrease significantly with increasing quantum dot size. All these findings point to the key role of quantum confinement in modulating the properties of quantum dots, especially in the case of electronic and optical properties.

In recent years, MXene quantum dots (MXQDs) have emerged as a topic of considerable interest due to their intriguing photoluminescent and absorption properties, which differ significantly from those of 2D MXenes. MXQDs exhibit absorption across a wide range of the electromagnetic spectrum, from UV to near-infrared (NIR), with their electronic structure being highly tunable *via* surface functionalization as well as the size of the MXQDs.[14,31] For example, Xue *et al.*[32] synthesized Ti_3C_2 MXQDs with lateral sizes of 2.9, 3.7, and 6.2 nm, observing typical absorption of these MXQDs with maxima at 260 and 320 nm. Xu *et al.*,[33] observed a size-dependent shift in the absorption spectrum, with $Ti_3C_2T_x$ MXQDs of 1.8, 2.5, and 3.3 nm showing absorption maxima at 324, 271, and 262 nm, respectively. Moreover, the introduction of heteroatom doping has further expanded the optical tunability of MXQDs. Xu *et al.*[34] reported co-doped S, N-$Ti_3C_2T_x$ QDs with sizes in the range of 2 and 17 nm, which exhibited multicolor luminescence in the blue, yellow, and orange regions. The absorption spectra, peaking below 360 nm, were strongly influenced by the type of doping heteroatom and the size of the QDs (with strong absorption peaks at 300 nm and 240 nm). Isapour *et al.*[35] likewise confirmed that different heteroatoms (N, S, and N + S) significantly affect the UV–Vis absorption of MXQDs, leading to distinct shifts of absorption peaks (317–338 nm) and broader absorption bands compared to undoped MQDs. Ramírez *et al.*[36] have experimentally and theoretically explored the impact of particle size, transition metals, and surface terminations on the energy gap and absorption spectra of MXQDs. Several analytical techniques, such as X-ray photoelectron spectroscopy (XPS), can characterize the type of functional groups on the surface. The type of attached functional groups depends on the etching chemicals used during the synthesis of the 2D MXenes. However, in most cases of MXQDs, the groups observed on the surface are –O, –F, –OH, –Cl, and/or –NH, where –O and –F groups predominate. The effect of the size of MXQDs on the electronic properties was also observed in the case of Ti_3C_2 QDs, where it was revealed that with increasing lateral size, the energy gaps with H passivation range from 2.76 eV (449.22 nm) to 1.14 eV (371.21 nm).[37] In addition, Feng *et al.*[38] revealed that decreasing the size of Ti_2C-MXene quantum dots leads to a significant increase in absorption due to a stronger quantum confinement effect. They observed that Ti_2C MXQDs with lateral sizes of 2.2 and 3.9 nm exhibited absorption in the IR region around 1500–1600 nm. Furthermore, our previous studies have also revealed a significant effect of size on the electronic as well as magnetic properties of MXQDs.[39] We have discovered that the energy gap in the non-magnetic Ti_2CO_2 QDs varied from 4.89 eV (253.55 nm) to 3.34 eV (371.21 nm) with particle size, and also that the electronic properties can be tuned by modifying the MXQDs edge. While several experimental studies have demonstrated the strong dependence of the optoelectronic properties of MXQDs on several factors such as size, surface termination, and transition metal composition,[40–42] the theoretical understanding of the microscopic mechanisms underlying these phenomena remains limited. However, for its usefulness, the calculations should be both precise and computationally tractable for nanostructures of at least 1 nm in size. A suitable methodology in terms of tractability could be time-dependent density functional theory (TDDFT).

To the best of our knowledge, no study has so far provided a detailed theoretical investigation of the optical properties of MXQDs using TDDFT, nor has the effect of surface functionalization on their optical response been systematically explored. In this context, we decided to investigate the effect of functionalized atoms/groups Ti_2CT_2 QD (where T = O, F, and –OH) as well as size (in the case of Ti_2CO_2 QD) on their electronic and optical properties using this method. In this work, we constructed MXene quantum dots (MXQDs) with different surface saturation (without edge functionalization, partially saturated, and fully saturated) to verify the stability of the investigated models. Specifically, we explore how variations in surface termination and MXQD size influence the energy gap, optical gap (the first optical transition), and exciton binding energy in these MXQDs. For all groups studied, stability was confirmed by binding and Gibbs energies, with the most stable structure observed at the fully saturated edge for all surface terminations. In the case of the effect of functionalization, we observe a significant decrease in the energy gap from 4.89 eV for Ti_2CO_2 to 4.49 and 3.90 eV for Ti_2CF_2 and $Ti_2C(OH)_2$, respectively. At the same time, a significant shift in the absorption spectrum was observed, where for F and OH functionalization, we observe absorption with a maximum in the visible region (around 320 nm) and the first clear optical transition in the near-infrared (NIR) region. On the contrary, in the case of Ti_2CO_2, the dominant absorption is in the near UV region with an absorption maximum of around 200 nm, while the first transition is observed around 750 nm (visible region). The study further reveals a clear size dependence of the optical properties of MXQDs, with larger quantum dots exhibiting a pronounced redshift in the absorption spectrum (around 900 nm for the biggest quantum dots) due to reduced quantum confinement effects. In addition, this work provides a deeper understanding of excitons in MXQDs and their relation to the optical response. We show that O-terminated MXQDs favor

more delocalized, charge-transfer-like excitons, while F- and OH-terminations promote localized excitons with stronger electron–hole overlap. We further find that the exciton binding energy decreases with increasing quantum dot size, accompanied by a larger average electron–hole separation, consistent with quantum confinement. Taken together, these findings highlight the tunability of the optical properties of MXQDs, where both surface functionalization and quantum dot size serve as effective parameters to control their optical behavior.

2 Computational methods

Ground-state optimal geometries and subsequent excited-state energies (in the ultraviolet and visible ranges) were simulated using density functional theory (DFT) and time-dependent DFT (TDDFT), employing the long-range hybrid ωB97XD[43] exchange–correlation functional and the 6-31G** [44] Pople basis set, as implemented in the Gaussian 16 software package.[45] The suitability of the 6-31G** basis set was validated in a previous study, where we demonstrated that this computationally efficient basis set produces an energy gap comparable to that obtained with the larger and more computationally demanding Dunning basis sets (*e.g.*, polarized valence triple-zeta cc-pVTZ).[39] Furthermore, this approach – including the choice of the ωB97XD functional – has been confirmed as adequate for modeling vertical absorption spectra, including charge transfer transitions.[46–49] Vibrational frequency calculations were performed on the optimized geometries to confirm they correspond to true minima on the potential energy surface. The RMS gradient strength criterion for geometry optimization was set to 3.0×10^{-4} in atomic units in the geometry optimization case. To assess the thermodynamic stability of the investigated Ti_2CT_2 quantum dots (QDs) and to compare the stability of different shapes (varying in the number of terminal atoms), the binding energy (E_b), the zero-point energy-corrected binding energy (E_0), and the Gibbs free energy (G) were calculated using the following equations:

$$E_{b/0} = (E_{MXQD} - (E_B + nE_T))/N \quad (1)$$

$$G = (G_{MXQD} - (G_B + nG_T))/N \quad (2)$$

where subscript MXQD denotes the Ti_2CT_2 (with functionalization), subscript B corresponds to the bare Ti_2C QD without functionalization, subscript T denotes isolated terminal atoms and/or group (O, F and/or OH), n is the number of isolated terminal atoms/groups (24, 30 or 36 atoms/groups) and N is the total number of atoms in MXQDs. The Gibbs free energies were calculated using Gaussian 16 with default settings at a temperature of 298.15 K. The energy gap Δ_g [eV] is defined as:

$$\Delta_g = \varepsilon_{LUMO} - \varepsilon_{HOMO}, \quad (3)$$

where ε_{LUMO} and ε_{HOMO} correspond to the eigenvalues of the lowest unoccupied molecular orbital (LUMO) and the highest occupied molecular orbital (HOMO), respectively. The nature of the excited states predicted by TDDFT was analyzed in terms of the most prominent natural transition orbitals (NTOs),[50] calculated using Gaussian 16. NTOs provide a compact representation of the transition density matrix, isolating each optical transition to one or two key particle–hole pairs that describe the main features of the excitation. This transformation is performed by applying a singular value decomposition to the transition density matrix D^{0I}, connecting the ground state (0) with the Ith excited state (I):

$$D^{0I} = Udiag(\sqrt{\lambda_1, \lambda_2, \ldots})V^T \quad (4)$$

where U denotes a set of initial (hole) orbitals, and V denotes the final (particles/electrons) orbitals. The λ_i reflects the contribution of a specific particle–hole transition to the overall excitation. Higher values correspond to dominant transitions, indicating that a particular particle–hole pair contributes more significantly to the electronic excitation. By focusing on the largest eigenvalues, the NTO framework reduces the transition density matrix to a minimal set of significant particle–hole pairs, offering a clear and concise depiction of the excited-state character and facilitating the interpretation of complex electronic excitations. Visualizations of the natural transition orbitals were generated using GaussView, version 6.[51] In addition, hole–electron distribution analysis was performed with the Multiwfn program (version 3.8), providing complementary insight into the spatial localization of the electron and hole.[31,52] Further quantitative analysis of the excited states, in particular in terms of the average hole–electron distance, was performed using the software TheoDORE.[53] Using TheoDore, it was possible to calculate an average hole–electron distance, defined as the root-mean-square separation between the electron and hole positions, quantified through the one-particle transition density matrix (1TDM). This approach estimates the spatial extent of the exciton by summing over all pairs of atoms M and N, weighted by the probability Ω_{MN} that the electron and hole are localized on these atoms, respectively. This average hole–electron distance is constructed for a particular optical transition as:

$$d_{he} = \sqrt{\sum_{M,N} \Omega_{MN} \cdot d_{MN}^2 / \Omega} \quad (5)$$

where d_{MN} represents the distance between atoms M and N on which the electron and hole are localized, and Ω is the norm of the exciton wavefunction, representing the overall probability distribution of the exciton, and this result is expressed in Å. However, it should be noted that this value will be significantly smaller than the real size of the exciton.

To verify and confirm the presence and the location of excitons in MXQDs, we performed additional TDDFT and GW + Bethe–Salpeter equation (BSE) calculations using the plane-wave Vienna *ab initio* simulation package (VASP) with the projector augmented wave (PAW) method.[54,55] These calculations and follow-up exciton wavefunction visualizations (by VESTA software[56]) were carried out firstly for the two-dimensional

Ti_2CO_2 MXene sheet as a reference system and subsequently for the smallest Ti_2CO_2 QD.

3 Results and discussion

In studying the optical properties of MXene quantum dots (MXQDs), we build on a previous study that revealed the effects of edge functional groups as well as the size of MXQDs on their electronic properties.[39] Therefore, in this study, we investigate for the first time the influence of surface termination and MXQD size on the optical properties of MXQDs using time-dependent density functional theory (TDDFT). Given the tendency of 2D MXenes to terminate with O, F, or OH groups,[8,9,57] we have selected surface oxygenation, fluorination, and hydroxylation as the primary functional groups. To further distinguish and characterize the studied MXQDs, the following notation is used: Ti_2CT_2 (T = O, F, OH) denotes the surface functionalization of MXQDs. Due to computational limitations, the smallest MXQD size with lateral sizes of 11.3–12.0 Å, containing 24 Ti atoms, 7 C atoms, and 36 functional atoms/groups, was selected for functional group analysis. In the part of the study on the size-dependence, Ti_2CO_2 QDs were selected from the previous study[39] and hereafter referred to as QD1, QD2, and QD3 with lateral sizes of 11.3, 13.3, and 17.5 Å, respectively. QD2 was constructed as an intermediate (asymmetric) geometry between the two symmetric QDs (QD1 and QD3) in order to enable comparison of different sizes within computationally feasible models. It should be noted that in a previous study,[39] a magnetic state was identified as the ground state of the smallest MXQDs (QD1); however, strong spin contamination was observed in the case of edge fluorination and hydroxylation, which complicates the accurate determination of the ground state. At the same time, the magnetic character disappears with increasing lateral size, and in the case of QD3, the ground state is a singlet with zero magnetic moments. Therefore, given the experimental average size of MXQDs (approximately 5 nm), we restrict our investigation to singlet (non-magnetic) states for all QDs considered in this study.

3.1 Simulated MXQDs structures and optimization

Before discussing the optical properties of MXQDs, we conducted a comprehensive stability analysis of the MXQD structures with different MXQD surface termination models. The hexagonal structure $Ti_{24}C_7$ represents the bare model without surface functionalization (see Fig. S1), $Ti_{24}C_7T_{24}$ represents the model without edge functionalization, $Ti_{24}C_7T_{30}$ represents the partially saturated, and $Ti_{24}C_7T_{36}$ represents the fully saturated models and optimization was performed for all models (see Fig. S2–S4). The optimization procedure included a subsequent frequency analysis to ensure all Hessian eigenvalues were positive, verifying dynamic stability. Thermodynamic stability was further assessed through binding energy calculations and application of the maximum hardness principle.[58] To evaluate the thermodynamic stability of the investigated $Ti_{24}C_7T_x$ with a different number of terminal atoms/group (T_x, where x = 24, 30 and 36), the binding energy E_b, the binding energy corrected to the zero-point energy E_0, and the Gibbs free energy G were calculated according to eqn (2) and (3) given in the section 2. Based on these definitions, negative values of E_b and G represent a spontaneous reaction that leads to higher stability of the product as a reactant, and a more negative value indicates a more energetically favorable (spontaneous) reaction. Table 1 shows that all investigated structures of $Ti_{24}C_7T_x$ QDs are thermodynamically stable (negative values of E_b and G for all structures). The negative Gibbs energy also indicates that MXQD formation is an exothermic (spontaneous) reaction for all types of functionalization. At the same time, it is evident that the fully saturated ($Ti_{24}C_7T_{36}$) QDs are more stable for all types of functionalization (T = O, F, and/or OH). The stability is also confirmed by the maximum hardness principle, based on which a molecule with a higher HOMO–LUMO energy gap is associated with greater stability. From Table 1, it is evident that saturated systems increase Δ_g compared to the corresponding bare structure (3.31 eV), with the highest value corresponding to fully saturated MXQDs. It is also worth noting the pronounced deformation of $Ti_{24}C_7T_{24}$ QD (without edge functionalization), and partially saturated ($Ti_{24}C_7T_{30}$) of the structures where the Ti–T bonds are elongated on the side of the QDs and subsequently shifted to the edge (see Fig. S2–S4). This appears to be an attempt to compensate for the lack of electrons on the edge after 0D reduction, suggesting a more likely full functionalization of the QD edge. In contrast, we observe that in the case of fully saturated QDs, there is no significant disruption of the hexagonal structure of the 2D Ti_2CT_2 monolayer and only a slight elongation of the Ti–T bond on the lateral side occurs after shrinkage to QDs. Based on these results, only fully saturated MXQDs structures were considered in the following part of the

Table 1 Binding energies E_b [eV per atom], zero point corrected relative energy E_0 [eV per atom], G Gibbs free energy change [eV per atom], and energy gap Δ_g [eV] of the $Ti_{24}C_7T_x$ of the various number of surface terminal atoms (T = O, F, and OH, x = 36, 30 and 24)

	O_{36}	O_{30}	O_{24}	F_{36}	F_{30}	F_{24}	$(OH)_{36}$	$(OH)_{30}$	$(OH)_{24}$
E_b	−4.42	−4.18	−3.84	−3.78	−3.41	−3.09	−3.25	−2.72	−2.63
E_0	−4.37	−4.21	−3.81	−3.76	−3.39	−3.07	−3.11	−2.63	−2.56
G	−4.15	−4.01	−3.62	−3.53	−3.18	−2.89	−2.93	−2.39	−2.35
Δ_g	4.89	4.58	4.02	4.48	4.46	4.03	3.90	3.70	3.51

The label in the table represents the type and number of terminal atoms.

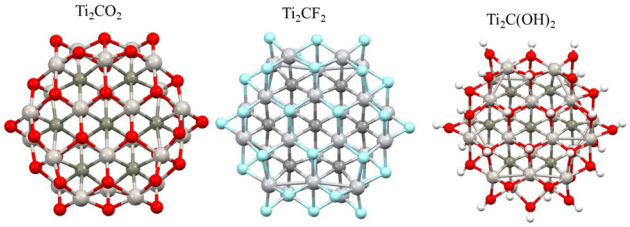

Fig. 1 Optimized structure of fully saturated Ti_2CT_2 MXQDs with different functionalization (T = O, F and OH). Titanium, carbon, oxygen, fluorine, and hydrogen atoms are shown in light grey, dark grey, red, blue, and white, respectively.

study (see Fig. 1), which will be hereafter denoted as Ti_2CT_2 (QD1) where T represents O, F, and/or OH.

Subsequently, the stability of different functional groups and their influence on the electronic properties of MXQDs were investigated. From the relevant values of E_b and G, it is clear that oxygen saturation is the preferred termination since the order decreases with the terminal group and the sequence is in the order Ti_2CO_2 < Ti_2CF_2 < $Ti_2C(OH)_2$ (see Table 1). The lowest values of E_b and G for the Ti_2CO_2 QDs may be due to the stronger interaction between the O and Ti atoms resulting from the shorter bond length of Ti–O, which ranges from 1.77 to 2.05 Å, than those of Ti–F from 1.90 to 2.22 Å and Ti–OH from 2.03 to 2.30 Å. Furthermore, in the context of the maximum hardness principle, where the molecule with the highest Δ_g can be considered the most stable, these results confirm previous findings, *i.e.*, that oxygenation can be considered the most probable surface termination. Our results reveal that the change in surface termination leads to a decrease in Δ_g from 4.89 eV for oxygenation to about 4.49 eV for fluorination and 3.90 eV for hydroxylation, as shown in Table 1 and Fig. 2. Note that although the infinite Ti_2CF_2 and $Ti_2C(OH)_2$ sheet is a gapless conductor,[8,9] their quantum dots have a non-zero energy gap, which is due to the quantum confinement. This result proves that the energy gap can be significantly tuned by chemical modification of Ti_2CT_2 QDs with different atomic and molecular groups. Our results are consistent with a previous study by Ramírez *et al.*,[36] which suggests that changing the functionalization on the surface of MXQDs causes a significant improvement in electronic properties.

Last but not least, in order to investigate the dependence of the electronic properties on the QDs size, we analyzed the Ti_2CO_2 MXQDs with a lateral size ranging from 11.3 to 17.5 Å (see Fig. 2). As expected, the energy gap decreases with increasing MXQDs size, while the HOMO and LUMO energies decrease and increase, respectively, consistent with the quantum confinement theory. A more pronounced decrease in the energy gap (approximately 1.5 eV) was observed between the smallest (QD1) and largest (QD3) QDs, as shown in Fig. 2. Interestingly, the change in the energy gap between QD1 and QD2 was relatively small (0.30 eV), probably due to the asymmetric growth of QD2, which did not significantly change the edge-to-area ratio (16% compared to 18% for QD1). This

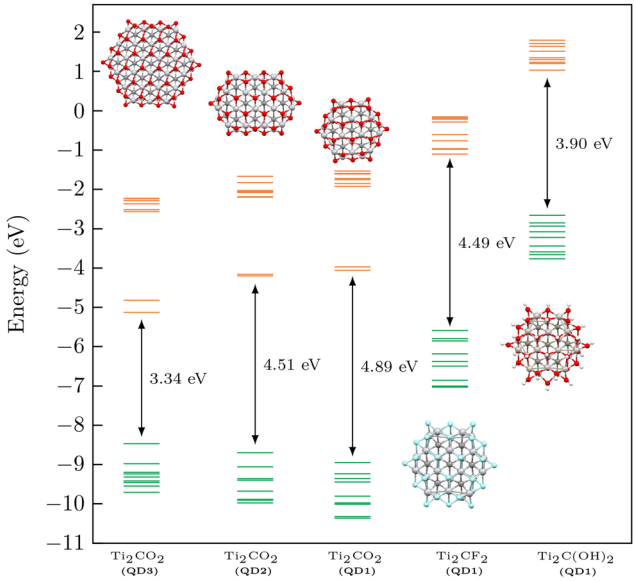

Fig. 2 Energy diagram of the occupied (green lines) and lowest unoccupied (orange lines) molecular orbital of the MXQDs model (a) with different surface functional groups and (b) with different lateral sizes. The Δ_g (in eV) values indicate the difference between the LUMO and HOMO.

suggests that the edge-to-area ratio plays a relevant role in determining the electronic properties of MXQDs.

3.2 Optical properties of MXQDs

In the second part of this study, we investigated the effect of surface functionalization and quantum dot size on the optical properties of selected MXQDs. Singlet excitation energies and optical spectra within the visible and near-UV regions (UV/Vis spectra) were computed using time-dependent density functional theory (TDDFT) at the ωB97XD/6-31G** level of theory, which was previously used to optimize the studied structures. However, for the larger quantum dot (QD3), due to the increased computational demands, the LanL2DZ basis set with effective core potentials (ECPs) was employed. This choice allowed us to reduce the computational cost while still maintaining the necessary accuracy to capture the relevant electronic and optical properties of the system (see Fig. S5). To ensure comprehensive coverage of the absorption spectrum at least accurately capture the Δ_g region (derived from the ground-state DFT calculations), an initial convergence analysis was conducted on the number of excited states in the TDDFT calculations. This step was crucial to ascertain that a sufficient range of electronic excitations is included, thereby providing a reliable representation of the absorption features. The analysis revealed that capturing the full absorption spectrum and accurately representing optical transitions around Δ_g for most quantum dots required at least 600 excited states. This level of excitation effectively covers the range of interest and captures optical transitions well beyond the Δ_g values observed at 254 nm, 277 nm, 318 nm and 274 nm for Ti_2CO_2, Ti_2CF_2, Ti_2C

$(OH)_2$ and QD2, respectively (see Fig. S6–S13). For QD3, which presents a notably lower energy gap (371 nm) and diminished excitonic effects (as elaborated in the following section), 200 excited states proved sufficient to comprehensively characterize its electronic (optical) transitions and capture the complete absorption spectrum (see Fig. S14 and S15).

3.2.1 Various surface functionalization of MXQDs. The calculated absorption spectra of MXQDs with different surface functionalizations (with a lateral size corresponding to QD1) are shown in Fig. 3.

These theoretical absorption spectra reveal a clear dependence on functionalization with distinct red shifts observed for Ti_2CF_2, $Ti_2C(OH)_2$ compared to Ti_2CO_2. Fig. 3 indicates that both groups exhibit an absorption onset around 800 nm, with maximum absorption peaks at approximately 340 nm for Ti_2CF_2 and 320 nm for $Ti_2C(OH)_2$, respectively. It is clear that the absorption maximum is near the energy gap in the case of $Ti_2C(OH)_2$, while in the case of Ti_2CF_2 it is prior to the energy gap. In contrast, the Ti_2CO_2 begins to absorb light around 400 nm, with its absorption maximum at 220 nm, significantly beyond its energy gap. These results indicate that its absorption primarily occurs in the UV region, with only a limited impact on the visible spectrum (see Fig. 3). Further differences arise in the near-infrared (NIR) region, where the $Ti_2C(OH)_2$ displays a prominent absorption peak around 1250 nm, with an oscillator strength of approximately 9% of the maximum value, indicating a strong NIR response (see Fig. 3 and S18). In contrast, both Ti_2CO_2 and Ti_2CF_2 show only a weak optical transition with a low oscillatory strength, which reaches approximately 3% of the maximum value (see Fig. S16 and S17). Due to the low value of the oscillatory strength, it is negligible and is not observed in the total absorption spectrum (see Fig. 3). Therefore, in the following analysis, only those transitions with oscillator strengths exceeding 3% of the maximum value are considered bright transitions.

A detailed description of the optical transitions is provided by Fig. 4, where, in addition to the bright optical transitions, we can also observe the presence of a dark optical transition.

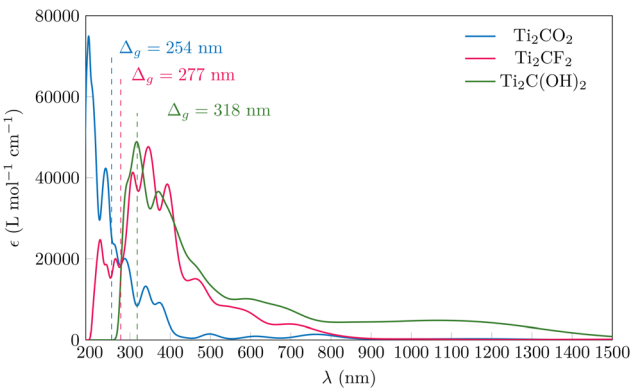

Fig. 3 Calculated absorption spectra (a molar absorption coefficient ε) of the QD1 with different surface functional groups. The envelope function assumes Gaussian broadening of peaks with σ = 0.15 eV.

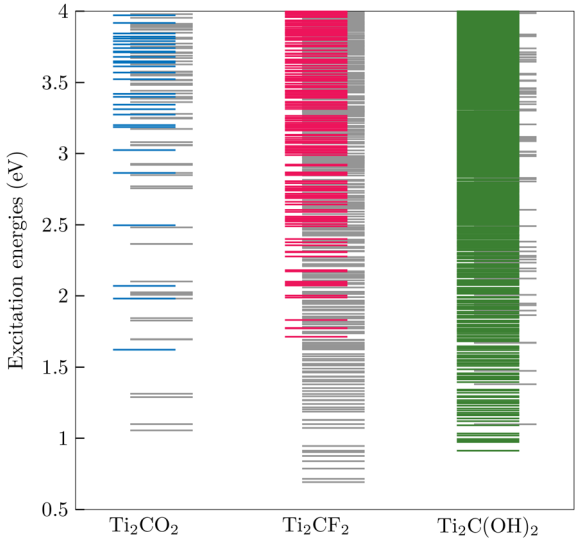

Fig. 4 Excitation energy levels for Ti_2CO_2, Ti_2CF_2, $Ti_2C(OH)_2$ QDs. Dark optical transitions (gray markers) indicate states with limited interaction with light, while bright optical transitions (colored markers) highlight states with strong optical activity.

From Fig. 4 it appears that a significant number of bright optical transitions with relatively high oscillatory strength in the case of $Ti_2C(OH)_2$ can be observed in the whole VIS and NIR (1.0–3.1 eV) region. Conversely, in the case of Ti_2CO_2, the first bright optical transition is observed at 1.62 eV (760 nm), although an increase in optical transitions with significant oscillatory strength (above 45% of the maximum value) is observed in the near-UV region between 3.2 and 6 eV (200–400 nm) (see also Fig. S10 and S21). The most interesting situation is observed in the case of Ti_2CF_2 QD, where the first bright excitation transition is observed in the visible range around 1.71 eV (720 nm). However, in contrast to Ti_2CO_2 QDs, a significant number of dark optical transitions are observed in the NIR region, suggesting the presence of hidden states that could influence the exciton dynamics and potentially transform into bright states under certain conditions. From the obtained results, it is evident that the optical properties of Ti_2C-based MXQDs are strongly dependent on the surface functional groups, and the calculated absorption spectra clearly show that functionalization plays a key role in tuning absorption in both the UV/Vis and NIR regions.

3.2.2 The size of MXQDs. The effect of MXQDs' size on the optical properties of oxygen-functionalized Ti_2CO_2 QDs was subsequently investigated. The calculated optical absorption spectra in Fig. 5 follow the trends observed above for the energy gap. The spectra show a pronounced blue shift with decreasing MXQDs sizes, with an onset at approximately 400 nm and a pronounced absorption peak at 220 nm for the smallest Ti_2CO_2 QDs (hereafter referred to as QD1), as described above. In contrast, in the case of the largest quantum dot (QD3), we observe a prominent absorption peak around 1200 nm that extends into the near-infrared region

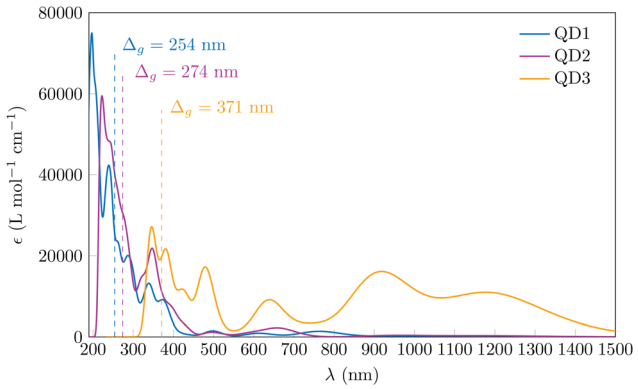

Fig. 5 Calculated absorption spectra (a molar absorption coefficient ε) of the Ti_2CO_2 QDs with different lateral sizes. The envelope function assumes Gaussian broadening of peaks with σ = 0.15 eV.

(NIR) (see Fig. 5 orange line). These observations are consistent with previous experimental work where absorption at 1500 nm was experimentally measured for Ti_2C QDs with a size above 2 nm.[38] In the case of QD2, small shifts towards higher wavelengths can be observed along with slight changes in the shape of the absorption spectrum, where we observe an increase in absorption at about 350 nm. In addition, upon closer examination of the optical transitions, we can observe a marked difference when comparing QD1 and QD3, as shown in Fig. S22. In the case of QD3, we observe both light and dark optical transitions already in the NIR region, *i.e.*, in the range from 0.7 to 1.6 eV (1780–776 nm) with a significant oscillatory strength (approximately 60% of the maximum value) (see Fig. S15 and S22). On the contrary, in the case of QD1, as mentioned above, we observe a more pronounced increase in the region above 3 eV with a maximum absorbance in the near-UV region. When examining the optical transitions, there is also a more pronounced similarity between QD1 and QD2, where we see a marked similarity in the distribution of bright and dark optical transitions. In the case of QD2, several dark optical transitions can also be observed in the range of 1.5 to 2.0 eV (826 to 413 nm), but the first bright optical transition is observed at 1.88 eV (663 nm) (see Fig. S13). This may be due to the lack of resizing (shape) of the QDs, as discussed above, resulting in a negligible change in the optical properties of the MXQDs. Our results are consistent with previous experimental studies showing a blue shift when the size of QDs is decreased.[20,27] In addition, the similarity in optical response between QD1 and QD2 suggests that small differences in size may have a limited effect on optical properties, especially when shape modifications are minimal.

3.3 Excitons in MXQDs

Excitons are electron–hole quasiparticles formed when an electron in the conduction band and a hole in the valence band bind together through Coulomb attraction. In low-dimensional materials and systems with weak dielectric screening, excitons play a crucial role in light absorption, light emission, and charge transport. Their key parameter is the exciton binding energy (E_{EB}), defined as the difference between the fundamental gap (Δ_G) and the optical gap (Δ_g^{opt}, the first bright transition). The fundamental gap is the difference between the energy to create a hole (remove an electron, the ionization potential) and the energy to add an electron (the electron affinity), while the optical gap corresponds to the excitation energy of a bound electron–hole pair (exciton) stabilized by the Coulomb interaction. A large E_{EB} indicates that excitons are stable and more difficult to dissociate into free carriers, a common feature of confined low-dimensional systems.[59]

In this work, we approximate the fundamental gap using the HOMO–LUMO gap (energy gap, Δ_g) derived from one-electron orbitals within the framework of hybrid density functional theory. Based on our results, we find significant differences between Δ_g and Δ_g^{opt} in all studied MXQDs. This notable difference suggests the presence of excitons with total delocalization across the molecule due to the quantum confinement effect. Subsequently, the "approximate" exciton binding energy ($\tilde{E}_{EB}$) is calculated as the difference between the energy gap and the optical gap. Despite these approximations, the approach provides valuable insights into trends in exciton and the influence of factors such as quantum dot size and functional groups on exciton binding energy. Table 2 summarizes the energy gap ($\Delta_g \approx \Delta_G$, approximate fundamental gap), optical gap (first optical transition, Δ_g^{opt}), and their associated values for the first exciton binding energy (its difference, $\tilde{E}_{EB}$) for all studied MXQDs models. It is evident that in all the models investigated, the first optical transition occurs at an energy significantly lower than the electronic gap. We observe that the exciton binding energy decreases with increasing MXQD size, because the exciton is forced to remain delocalized throughout the molecule due to its limited spatial dimensions in the case of small quantum dot sizes. Using TheoDore software, it was possible to calculate the average distance between the instantaneous position of the electron and the hole (d_{he}). This analysis showed that the average hole–electron distance increases proportionally with the size of the MXQD, as shown in Table 2. This is expected based on previous findings showing that in smaller quantum dots, the exciton is bound more tightly, leading to a higher exciton binding energy.[27] As the size of the quantum dot increases, the exciton can occupy more space,

Table 2 The MXQDs radius r_{MXQDs} [Å], the energy gap Δ_g [eV], the optical gap (frist bright optical transition) Δ_g^{opt} [eV], the exciton binding energy $\tilde{E}_{EB}$ [eV], and the average hole–electron distance (d_{he} [Å]) for the first bright optical transition of MXQDs with different surface functionalization and size

	r_{MXQDs}	Δ_g	Δ_g^{opt}	$\tilde{E}_{EB}$	d_{he}	$\tilde{E}_{EB}/\Delta_g$
Ti_2CO_2 (QD1)	5.66	4.89	1.62	3.27	4.34	67%
Ti_2CO_2 (QD2)	6.55	4.51	1.87	2.64	4.56	59%
Ti_2CO_2 (QD3)	8.73	3.25	1.04	2.12	5.40	65%
Ti_2CF_2 (QD1)	6.00	4.48	1.71	2.77	3.37	62%
$Ti_2C(OH)_2$ (QD1)	6.02	3.90	0.91	2.92	3.50	75%

which is reflected by a decrease in exciton binding energy and a simultaneous increase in size.

The optical transition can be expressed using a single pair of orbitals by transforming the normal orbital representation into a more compact form known as the natural transition orbitals (NTOs). In Fig. 6, the dominant NTO pairs involved in the first optical transition of MXQD are shown with their respective probabilities. In Ti_2CO_2, the NTO analysis reveals that in the largest quantum dot (QD3), the hole NTO is mainly localized in the center of the structure, whereas with decreasing size down to QD1, the hole NTO becomes delocalized across the entire dot as a consequence of the confinement effect. The particle NTO, in contrast, remains concentrated near the edges for all sizes. In the smallest Ti_2CO_2 QD1, the strong confinement forces the exciton into a compact spatial region, which enhances the Coulomb interaction and results in a high exciton binding energy. These conclusions are further supported by the charge-density difference (CDD), which compares the first excited state with the ground state and delineates spatial regions of electron-density accumulation and depletion. To characterize the spatial co-localization of the hole and electron, the overlap function $S_r(r)$ is used; its integral yields the dimensionless S_r index (0–1; lower values indicate spatial separation, higher values strong local overlap). A detailed description of definitions and computational procedures is provided in the literature Liu *et al.*[60] and the manual for the Multiwfn 3.7 (dev) code[61] (see Fig. S28 and S29). For Ti_2CO_2 QD1, the heat map shows that the hole is strongly localized on the central carbon atom with partial contributions from titanium atoms, whereas the electron is distributed over the edge carbons with a slight contribution on oxygen and titanium atoms. As shown in Fig. 7, a slight electron–hole overlap is observed across the entire molecule, predominantly on carbon atoms, with partial contributions on titanium and oxygen, consistent with a broadly delocalized excitonic character in Ti_2CO_2 QD1. In contrast, in Ti_2CO_2 QD3, both hole and electron are localized in the central region of the quantum dot, predominantly on carbon atoms, leading to a stronger overlap. This effect is quantified by the S_r index,

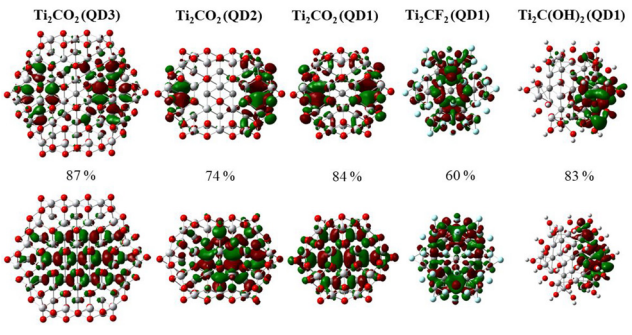

Fig. 6 Dominant NTO pairs involved in the first optical transition of the MXQDs with different sizes and different functionalization. For this transition, the "hole" is at the bottom, and the "particle" (excited electron) is at the top; values represent the percentage of the respective NTO pairs.

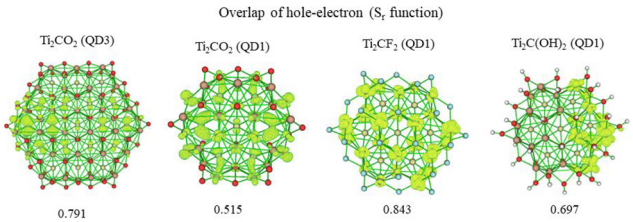

Fig. 7 Spatial map of the hole–electron overlap $S_r(r)$ for the first optical transition, together with the corresponding S_r index, presented for the selected QDs. The isosurface value is 0.001 e Å^{-3}.

which increases from 0.515 in Ti_2CO_2 QD1 to 0.791 in Ti_2CO_2 QD3 (see Fig. 7), directly reflecting the enhanced electron–hole overlap in larger dots. The stronger overlap lowers the exciton binding energy and stabilizes lower-energy states, thereby explaining the redshift of the absorption spectrum into the visible and NIR regions. Similar trends with a decrease in the exciton binding energy and a concomitant increase in the average hole–electron distance with increasing QD size have been observed in previous studies, confirming the consistency of our findings with the observed quantum confinement effects.[27–29]

Surface functionalization leads to pronounced changes in the spatial distribution of the hole and electron for the first optical transition. In Ti_2CO_2, the hole NTO is delocalized across the dot, while the electron NTO extends over the carbon framework and toward the edges, giving rise to a delocalized exciton. In contrast, fluorine and hydroxyl terminations induce stronger localization: in Ti_2CF_2, both hole and electron densities cluster around central Ti atoms, producing a compact, core-localized exciton, while in $Ti_2C(OH)_2$ they are predominantly concentrated on Ti atoms at the edges, yielding an edge-localized exciton (Fig. 6). This localization shortens the average hole–electron distance d_{he} (3.37 Å for Ti_2CF_2, 3.50 Å for $Ti_2C(OH)_2$) relative to oxygen termination (4.34 Å for Ti_2CO_2). In line with these observations, the exciton binding energy is highest for Ti_2CO_2 (3.27 eV) and lower for Ti_2CF_2 (2.77 eV) and $Ti_2C(OH)_2$ (2.99 eV) (Table 2). These trends are consistently supported by the atomic-contribution heat maps and CDD plots (Fig. 7, S28 and S29), which illustrate how functionalization modifies the localization of hole and electron for the first optical transition. As noted above, for Ti_2CO_2 the electron–hole pair is distributed across the entire molecule, with an overlap of S_r = 0.515, predominantly on carbon atoms and partly on titanium and oxygen. A different situation arises upon changing the surface functionalization: in Ti_2CF_2, both the hole and the electron are predominantly localized on Ti atoms, yielding a large overlap of S_r = 0.843. A similar situation is observed for the OH termination, where the overlap is localized on Ti atoms at the edges of the molecule and attains an intermediate value of S_r = 0.697. In both cases, the electron–hole overlap is strongly localized on Ti atoms, whereas the functional groups (F and OH) contribute to the first optical transition only negligibly (see Fig. 7). This behavior originates

from the high electronegativity of fluorine and the polarizing effect of hydroxyl groups, which alter Ti–T bonds and draw charge density toward Ti, thereby reducing delocalization. Consequently, O termination favors delocalized excitons with predominantly UV absorption, whereas F and OH terminations promote localized states that shift absorption into the visible and NIR regions.

Another view on the excitons can be provided by the analysis of the full excitonic wavefunction written as a function of coordinates of two particles ($\mathbf{r}_e$ for an electron and $\mathbf{r}_h$ for a hole) $\psi_\lambda(\mathbf{r}_e, \mathbf{r}_h) = \sum_{cv} A^\lambda_{cv} \phi^*_c(\mathbf{r}_e)\phi_v(\mathbf{r}_h)$, where the BSE (or TDDFT) eigenvectors A^λ_{cv} correspond to the amplitudes of free electron–hole pair configurations composed of electron states ϕ_c and hole states ϕ_v (v and c means valence and conduction bands, respectively). We therefore firstly performed a full Bethe–Salpeter equation (BSE) calculation on semiconducting Ti_2CO_2 monolayer MXene, to check the natural behavior of excitons without space limits. This type of accurate calculation on top of the many-body perturbative GW method is possible only in a small computational cell (here, the unit cell of 2D Ti_2CO_2 contains five atoms). We recently successfully applied such a method to other semiconducting monolayer MXenes, and also, comparisons to the independent FNDMC method were done.[62–64] The provided quantities are (among others) the fundamental gap, optical gap, and binding energy of the first bright exciton.

When one iterates GW eigenvalues (evGW variant of GW method), as discussed in our previous work,[39] both direct and indirect gaps are significantly opened: Δ^{dir}_{GW} = 1.82 eV → 2.48 eV and Δ^{indir}_{GW} = 1.32 eV → 1.82 eV, respectively. Further, the optical gap from subsequent BSE is changed as Δ^{opt}_{BSE} = 1.26 eV → 1.78 eV. We note that our GW calculations with a "standard" setting[65] were renormalized to well-converged, precise values of G_0W_0 of Ding *et al.*[37] (as explained in Table S1 of SI). The binding energy of the first bright exciton in 2D Ti_2CO_2 is therefore $E_{EB} = \Delta_{GW} - \Delta^{opt}_{BSE}$ = 0.69 eV which is approximately 28% of fundamental gap Δ_{GW}. This is in line with linear scaling in 2D materials $E_{EB} \approx \Delta_{GW}/4$, presented in ref. 66. Concerning the size of the first bright exciton in 2D Ti_2CO_2, it is necessary to consider at least 12 × 12 unit cells to fade out the wavefunction signal (Fig. 8a and b), *i.e.*, we guess an excitonic radius of about 24 Å.

For QD, it is not possible to use the same GW-BSE approach (at least not in plane-wave software forcing a big vacuum-containing simulation box, here 21 Å × 20 Å × 15 Å). We therefore used our previous trick how to recover the behavior of the accurate GW + BSE method: TD-HSE06 mimics quite well BSE + G_0W_0 optical properties of 2D materials,[67] including Ti_2CO_2 (TD-HSE06 optical gap 1.20 eV (ref. 3) *vs.* BSE + G_0W_0 1.26 eV (ref. 37)). As BSE + evGW is more appropriate for MXQD, and density functionals providing larger gaps than standard hybrid density functionals, rather long-range hybrid ones should be used for the modeling of Ti-based quantum dot systems, where GW cannot be used.[39] We therefore finally used TD-PBE0 implemented in VASP,[68] which mimics a 2D system quite well (BSE + evGW). Fig. 8 provides direct visual proof of artificial confinement of the Ti_2CO_2 exciton in the space provided by QD. In MXQD, the exciton is strongly limited in space; however, similar blobs of electron density as in the corresponding 2D material are visible (Fig. 8d, *cf.* to Fig. 8c). Such a confinement leads to extreme bias of the binding energy of excitons in MXQD with respect to its 2D counterpart. Despite we have only rough guesses of energy and optical gaps in MXQD (from DFT and TDDFT, respectively), the ratio $\tilde{E}_{EB}/\Delta_g$ is extremely huge: from 59% to 75% depending on MXQD terminations, see the last column of the Table 2. This is 2–3 times more than in corresponding 2D materials ($E_{EB}/\Delta_{GW} \approx 25\%$).

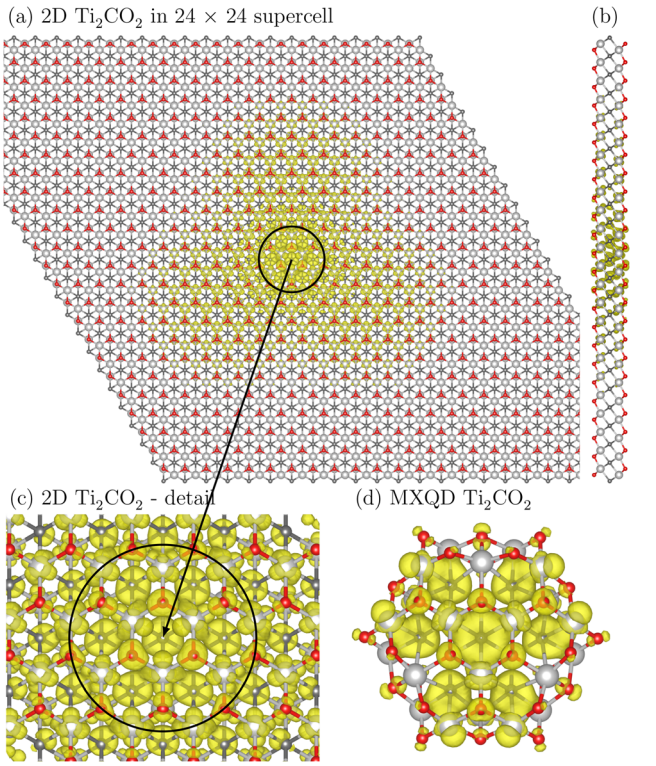

Fig. 8 The exciton wavefunction of the first bright exciton expressed as the real space electron probability density (yellow surface), where the hole is located at the top of Ti atom 1 Å away in the *z*-direction. The exciton in 2D Ti_2CO_2 material in (a) top view, (b) side view, and (c) detailed top view is compared to the (d) exciton in the Ti_2CO_2 quantum dot.

4 Conclusions

In this work, we employed time-dependent density functional theory (TDDFT) to systematically investigate the impact of surface functionalization and quantum dot (QD) size on the electronic and optical properties of Ti_2C-based MXene quantum dots (MXQDs). Our results demonstrate clear size- and termination-dependent trends in the absorption spectra, energy gaps, and excitonic effects. By directly comparing different surface terminations (O, F, and OH), we establish functionalization as a key factor in tailoring the optical response of MXQDs. Among the functionalizations investi-

gated, oxygen-terminated QDs (Ti_2CO_2) exhibited the highest stability and largest energy gap. In contrast, fluorine (Ti_2CF_2) and hydroxyl ($Ti_2C(OH)_2$) functionalizations reduced the energy gap and shifted absorption into the visible and near-infrared (NIR) regions. The largest Ti_2CO_2 QD, with a lateral size 17.46 Å, shows pronounced absorption in the near-infrared (NIR) region, whereas the shrinking of quantum dots results in a marked blue shift in the absorption spectrum due to enhanced quantum confinement effects. The study also revealed that exciton binding energy increases with decreasing QD size, while the average electron–hole distance decreases. Visualization of natural transition orbitals (NTOs) confirms that quantum confinement in smaller MXQDs produces more extended excitonic states. In larger QDs, both hole and electron densities localize with stronger overlap. Beyond size effects, surface functionalization has an even stronger impact on exciton character. O termination favors delocalized states with limited electron–hole overlap, which correlates with absorption predominantly in the UV region. By comparison, F and OH terminations induce Ti-centered localization (either in the core or at the edges), substantially enhancing electron–hole overlap. These trends are consistently reflected in the S_r index, which exhibits low values for O termination and markedly higher ones for F and OH. This directly links surface functionalization to exciton localization and to systematic red-shifts of the absorption spectrum into the visible and NIR regions. In any case, the excitonic effects are extremely huge in MXQD, much more than in 2D materials (which are also strong), because of the space confinement (which we also visually proved from the exciton wavefunction). The binding energy of the first exciton in MXQD can achieve up to 75% of its energy gap (in 2D materials, the typical value is around 25%), which critically influences (increases and shifts) optical absorption. These findings point to the significant tunability of the optical properties of MXQDs through surface functionalization and dimensional change. In terms of applications, O-functionalized MXQDs with large band gaps may be suitable for photocatalytic processes.[69] In contrast, OH-functionalized systems, with broadband absorption extending into the visible and NIR regions, show strong potential for photodetectors, solar cells, and bioimaging in the NIR biological window.[70] At the same time, further research should address challenges such as the controlled synthesis of well-defined MXQDs and the role of defects, which remain critical for fully realizing their application potential. In addition, exploring mixed functionalization strategies may provide further opportunities for optimizing and fine-tuning the optical properties of MXenes. At the same time, further research should address challenges such as the controlled synthesis of well-defined MXQDs and the role of defects, which remain critical for fully realizing their application potential.

Conflicts of interest

There are no conflicts to declare.

Data availability

The data supporting this article have been included as part of the supplementary information (SI). Supplementary information: detailed data for the calculated structures of Ti_2C and Ti_2CT_2 MXenes quantum dots, detailed data for the calculated absorption spectra: development of the necessary excited state, oscillator strengths, and excitation energy levels, detailed NTO and electron–hole analysis of the first optical transition for all studied structures. See DOI: **https://doi.org/10.1039/d5nr03127c**.

Acknowledgements

This article has been produced with the financial support of the European Union under the LERCO project (number CZ.10.03.01/00/22_003/0000003) *via* the Operational Programme Just Transition. The computations were performed at IT4Innovations National Supercomputing Center through the e-INFRA CZ (grant ID: 90254).

References

1 M. Naguib, M. Kurtoglu, V. Presser, J. Lu, J. Niu, M. Heon, L. Hultman, Y. Gogotsi and M. W. Barsoum, *Adv. Mater.*, 2011, **23**, 4248–4253.
2 B. Anasori and Y. Gogotsi, *Graphene 2D Mater.*, 2022, **7**, 75–79.
3 T. Ketolainen and F. Karlický, *J. Mater. Chem. C*, 2022, **10**, 3919–3928.
4 N. Kumar and F. Karlický, *Appl. Phys. Lett.*, 2023, **122**, 183102.
5 J. Kalmár and F. Karlický, *Phys. Chem. Chem. Phys.*, 2024, **26**, 19733–19741.
6 A. Bafekry, C. V. Nguyen, C. Stampfl, B. Akgenc and M. Ghergherehchi, *Phys. Status Solidi B*, 2020, **257**, 2000343.
7 T. Sakhraoui and F. Karlický, *Phys. Chem. Chem. Phys.*, 2024, **26**, 12862–12868.
8 B. Vénosová and F. Karlický, *Phys. Chem. Chem. Phys.*, 2024, **26**, 18500–18509.
9 M. Novotný, K. Tkáčová and F. Karlický, *Phys. Chem. Chem. Phys.*, 2024, **26**, 25514–25523.
10 S. Y. Lim, W. Shen and Z. Gao, *Chem. Soc. Rev.*, 2015, **44**, 362–381.
11 J. Feng, H. Dong, L. Yu and L. Dong, *J. Mater. Chem. C*, 2017, **5**, 5984–5993.
12 M. Bacon, S. J. Bradley and T. Nann, *Part. Part. Syst. Charact.*, 2013, **31**, 415–428.
13 M. Safaei and M. R. Shishehbore, *J. Mater. Sci.*, 2021, **56**, 17942–17978.
14 C. Zhou, K. B. Tan, W. Han, L. Wang and M. Lu, *Particuology*, 2024, **91**, 50–71.

15 P. Prabha Sarangi, D. Prava Sahoo, U. Aparajita Mohanty, S. Nayak and K. Parida, *ChemCatChem*, 2024, **16**, e202301533.
16 J. Ye, D. Gaur, C. Mi, Z. Chen, I. L. Fernández, H. Zhao, Y. Dong, L. Polavarapu and R. L. Z. Hoye, *Chem. Soc. Rev.*, 2024, **53**, 8095–8122.
17 H. Ali, Y. Orooji, B. A. Alwan, A. E. Jery, A. M. Abu-Dief, R. Al-Faze, S.-R. Guo, B. Wu and A. Hayat, *J. Energy Chem.*, 2025, **111**, 790–846.
18 Z. Yang and J. Wang, *Langmuir*, 2023, **39**, 4179–4189.
19 X. Guo, Z. Fan, Y. Wang and Z. Jin, *Surf. Interfaces*, 2021, **24**, 101105.
20 M. A. Zwijnenburg, *Phys. Chem. Chem. Phys.*, 2022, **24**, 21954–21965.
21 Sariga, A. M. Babu, S. Kumar, R. Rajeev, D. A. Thadathil and A. Varghese, *Adv. Mater. Interfaces*, 2023, **10**, 2202139.
22 H. Guan, S. Zhao, H. Wang, D. Yan, M. Wang and Z. Zang, *Nano Energy*, 2020, **67**, 104279.
23 G. Chen, Y. Zhang, C. Li and Q. Wang, in *Near Infrared Ag2S Quantum Dots: Synthesis, Functionalization, and In Vivo Stem Cell Tracking Applications*, Springer International Publishing, 2020, pp. 279–304.
24 C. B. Murray, D. J. Norris and M. G. Bawendi, *J. Am. Chem. Soc.*, 1993, **115**, 8706–8715.
25 X. Peng, J. Wickham and A. P. Alivisatos, *J. Am. Chem. Soc.*, 1998, **120**, 5343–5344.
26 M. Hines and G. Scholes, *Adv. Mater.*, 2003, **15**, 1844–1849.
27 E. Madden and M. A. Zwijnenburg, *Phys. Chem. Chem. Phys.*, 2024, **26**, 11695–11707.
28 J. M. Elward and A. Chakraborty, *J. Chem. Theory Comput.*, 2013, **9**, 4351–4359.
29 S. I. Pokutnii, *Semiconductors*, 2010, **44**, 488–493.
30 H. Ouarrad, F.-Z. Ramadan and L. B. Drissi, *RSC Adv.*, 2019, **9**, 28609–28617.
31 J. Liu, S. Chen, J. He, R. Huang, L. Tao, Y. Zhao and Y. Yang, *Nanomaterials*, 2022, **12**, 2043.
32 Q. Xue, H. Zhang, M. Zhu, Z. Pei, H. Li, Z. Wang, Y. Huang, Y. Huang, Q. Deng, J. Zhou, S. Du, Q. Huang and C. Zhi, *Adv. Mater.*, 2017, **29**, 1604847.
33 G. Xu, Y. Niu, X. Yang, Z. Jin, Y. Wang, Y. Xu and H. Niu, *Adv. Opt. Mater.*, 2018, **6**, 1800951.
34 Q. Xu, L. Ding, Y. Wen, W. Yang, H. Zhou, X. Chen, J. Street, A. Zhou, W.-J. Ong and N. Li, *J. Mater. Chem. C*, 2018, **6**, 6360–6369.
35 S. Isapour, M. Babazadeh-Mamaqani, H. Roghani-Mamaqani, A. Motalebnejad-Mamaqani, A. Rezvani-Moghaddam, H. Riazi, M. Salami-Kalajahi and M. Soroush, *J. Photochem. Photobiol., A*, 2025, **467**, 116446.
36 R. Ramírez, A. Melillo, S. Osella, A. M. Asiri, H. Garcia and A. Primo, *Small Methods*, 2023, **7**, 2300063.
37 Y.-M. Ding, X. Nie, H. Dong, N. Rujisamphan and Y. Li, *Nanoscale Adv.*, 2020, **2**, 2471–2477.
38 Z. Feng, G. Yiyu, J. Libin and W. Qiao, *Laser Photonics Rev.*, 2021, **15**, 2100059.
39 B. Vénosová and F. Karlický, *Nanoscale Adv.*, 2023, **5**, 7067–7076.
40 R. Madhushree and D. Pinheiro, *Opt. Mater.*, 2025, **166**, 117218.
41 Y. Huang, X. Wang, H. Zhang, L. Gao, J. Meng, Y. Liao, Q. Zhou, Y. Wei, B. Zong, H. Li and W.-L. Dai, *Appl. Catal., B*, 2025, **371**, 125262.
42 S. A. Althawab, A. Alzahrani, B. M. Alohali and T. Alsulami, *Colloids Surf., A*, 2025, **722**, 137291.
43 J.-D. Chai and M. Head-Gordon, *J. Chem. Phys.*, 2008, **128**, 084106.
44 V. A. Rassolov, M. A. Ratner, J. A. Pople, P. C. Redfern and L. A. Curtiss, *J. Comput. Chem.*, 2001, **22**, 976–984.
45 M. J. Frisch, G. W. Trucks, H. B. Schlegel, G. E. Scuseria, M. A. Robb, J. R. Cheeseman, G. Scalmani, V. Barone, G. A. Petersson, H. Nakatsuji, X. Li, M. Caricato, A. V. Marenich, J. Bloino, B. G. Janesko, R. Gomperts, B. Mennucci and D. J. Hratch, *Gaussian 16, Revision B.01*, 2016.
46 M. Sudolská, M. Dubecký, S. Sarkar, C. J. Reckmeier, R. Zbořil, A. L. Rogach and M. Otyepka, *J. Phys. Chem. C*, 2015, **119**, 13369–13373.
47 D. Jacquemin, B. Mennucci and C. Adamo, *Phys. Chem. Chem. Phys.*, 2011, **13**, 16987.
48 A. D. Laurent and D. Jacquemin, *Int. J. Quantum Chem.*, 2013, **113**, 2019–2039.
49 J.-C. Lee, J.-D. Chai and S.-T. Lin, *RSC Adv.*, 2015, **5**, 101370–101376.
50 R. L. Martin, *J. Chem. Phys.*, 2003, **118**, 4775–4777.
51 R. Dennington, T. A. Keith and J. M. Millam, *GaussView Version 6*, Semichem Inc., Shawnee Mission KS, 2019.
52 T. Lu and F. Chen, *J. Comput. Chem.*, 2011, **33**, 580–592.
53 F. Plasser, *J. Chem. Phys.*, 2020, **152**, 084108.
54 G. Kresse and D. Joubert, *Phys. Rev. B:Condens. Matter Mater. Phys.*, 1999, **59**, 1758–1775.
55 P. E. Blöchl, *Phys. Rev. B:Condens. Matter Mater. Phys.*, 1994, **50**, 17953–17979.
56 K. Momma and F. Izumi, *J. Appl. Crystallogr.*, 2011, **44**, 1272–1276.
57 R. Ibragimova, M. J. Puska and H.-P. Komsa, *ACS Nano*, 2019, **13**, 9171–9181.
58 R. G. Pearson, *Acc. Chem. Res.*, 1993, **26**, 250–255.
59 K. R. Hansen, J. S. Colton and L. Whittaker-Brooks, *Adv. Opt. Mater.*, 2023, **12**, 2301659.
60 Z. Liu, T. Lu and Q. Chen, *Carbon*, 2020, **165**, 461–467.
61 T. Lu, Multiwfn Software Manual (ver. 3.8). Available: **https://sobereva.com/multiwfn/** (accessed 25 September 2025).
62 M. Dubecký, F. Karlický, S. Minárik and L. Mitas, *J. Chem. Phys.*, 2020, **153**, 184706.
63 M. Dubecký, S. Minárik and F. Karlický, *J. Chem. Phys.*, 2023, **158**, 054703.
64 M. Kolos and F. Karlický, *J. Phys. Chem. C*, 2025, **129**, 2782–2787.
65 GW calculations by the VASP code using $N_B = 384$ number of bands (24 of them updated in GW), plane-wave energy cut-off $E_{cut} = 500$ eV, GW cut-off $E_{cut}^{GW} = 200$ eV, $\Delta z = 20$ Å distance to perpendicular image, and $18 \times 18 \times 1$ k-point grid.

66 Z. Jiang, Z. Liu, Y. Li and W. Duan, *Phys. Rev. Lett.*, 2017, **118**, 266401.
67 T. Ketolainen, N. Macháčová and F. Karlický, *J. Chem. Theory Comput.*, 2020, **16**, 5876–5883.
68 TD-PBE0 calculations by the VASP code using N_B = 320 number of bands (from them 90 occupied and 54 virtual for Casida (TD) part), plane-wave energy cut-off E_{cut} = 450 eV, simulation box of 21 Å × 20 Å × 15 Å, and Γ-point version of VASP.
69 A. Chakravorty and S. Roy, *Sustain. Chem. Environ.*, 2024, **8**, 100155.
70 Y. Cai, Z. Wei, C. Song, C. Tang, W. Han and X. Dong, *Chem. Soc. Rev.*, 2019, **48**, 22–37.